Physica Scripta

INCLUSIVE PUBLISHING TRUSTED SCIENCE

PURPOSE-LED PUBLISHING™

**PAPER** • **OPEN ACCESS**

# Constrained Hamiltonian realizability of thermoelectric Pareto spectra at finite power in coherent tight-binding chains

To cite this article: Mustafa Ali Çipiloğlu 2026 *Phys. Scr.* **101** 445922

View the article online for updates and enhancements.

You may also like

- ERRATUM: Critical quench dynamics of Wegner's $_2$ gauge model: a geometric perspective (2026 *J. Stat. Mech.* 103202)
Ramgopal Agrawal, Leticia F Cugliandolo and Marco Picco
- The Size of Particles Populating the Asymmetric Coma of Interstellar Comet 3I/ATLAS
Evgenij Zubko and Gorden Videen
- The Orbital Parameters of the Spectroscopic Binary WISPIT 2
H. Alqubelat, C. J. Bürgy, C. F. Manara et al.

This content was downloaded from IP address 194.27.50.18 on 14/11/2026 at 21:13

Physica Scripta

Check for updates

OPEN ACCESS

RECEIVED
9 September 2026

REVISED
6 October 2026

ACCEPTED FOR PUBLICATION
23 October 2026

PUBLISHED
5 November 2026

Original content from this work may be used under the terms of the Creative Commons Attribution 4.0 licence.

Any further distribution of this work must maintain attribution to the author(s) and the title of the work, journal citation and DOI.

PAPER

# Constrained Hamiltonian realizability of thermoelectric Pareto spectra at finite power in coherent tight-binding chains

**Mustafa Ali Çipiloğlu** *

Faculty of Engineering and Natural Sciences, Department of Physics, Manisa Celal Bayar University, Manisa, Türkiye
* Author to whom any correspondence should be addressed.

**E-mail:** ali.cipiloglu@cbu.edu.tr

**Keywords:** quantum thermoelectrics, Landauer transport, multiobjective optimization, coherent tight-binding chain, finite-power transport, spectral projection

Supplementary material for this article is available online

## Abstract

We quantify how a numerically optimized thermoelectric power-efficiency front changes when its transmission spectra are projected onto bounded coherent tight-binding chains. Finite-bias reservoir occupations are used with a static scattering Hamiltonian. Five independent smooth-spectrum searches are pooled and refined, and 30 targets are fitted to every chain length from three to eight sites. Spectral agreement and preservation of the operating point are assessed separately using pole-aware adaptive integration. A five-site chain gives small median transport-weighted spectral error, but spectral agreement alone does not ensure close efficiency agreement. A declared joint tolerance provides the smallest successful tested chain length along the front; the highest-power targets remain unresolved within the tested range and search budget. Doubling onsite and hopping bounds for the highest-power five-site target slightly improves the combined objective while increasing its operating-point distance. Numerical bias-profile comparisons, a one-sided shrinking-window Carnot test and current-noise diagnostics further delimit the results. The contribution is a reproducible, search-conditional spectral-to-Hamiltonian realizability map, rather than a new thermodynamic bound or a self-consistent finite-bias device prediction.

## 1. Introduction

Energy-selective transport is a central organizing principle of nanoscale thermoelectricity. In coherent conductors, charge and heat currents can be expressed through the energy-dependent transmission function within the Landauer–Büttiker framework [1–3]. This viewpoint has supported both general analyses of mesoscopic heat transport [4–6] and the search for transmission functions that optimize thermoelectric performance. The linear-response energy-filtering argument of Mahan and Sofo [7] and finite-power bounds derived by Whitney [8, 9] established benchmark constraints, while later variational and device-oriented studies clarified the role of boxcar and step-like transmissions [10, 11].

The gap between an optimal transmission function and a realizable microscopic structure remains a distinct design problem. A mathematically favorable $\mathcal{T}(E)$ need not be reproducible by a short Hamiltonian with bounded onsite energies, hoppings and contact broadenings. This distinction is increasingly relevant as inverse-design methods are brought into quantum transport. Automatic differentiation nonequilibrium Green-function methods, for example, can optimize Hamiltonian parameters against desired transport observables [12]; multiobjective evolutionary algorithms provide a complementary route when power and efficiency must be treated simultaneously [13]. The question addressed here is therefore not whether Hamiltonian inverse design is possible in principle, but how faithfully a thermoelectric Pareto set defined in a flexible spectral space can be projected onto a low-dimensional coherent architecture.

The physical scope must be stated carefully. Quantum-dot thermoelectrics often operate in regimes where charging, sequential tunneling, cotunneling or Kondo correlations are essential [14–18].

© 2026 The Author(s). Published by IOP Publishing Ltd

Experiments also demonstrate strongly nonlinear thermoelectric response and high-efficiency energy conversion in quantum-dot devices [19–22], while interacting theories show that charging can qualitatively modify nonlinear thermovoltage and heat dissipation [23]. The Hamiltonian used below contains none of these many-body effects. It is therefore described throughout as a non-interacting coherent tight-binding chain, not as a model of a Coulomb-blockaded gate-defined quantum dot. Likewise, finite-bias refers to exact reservoir occupations evaluated with a static scattering spectrum; bias-dependent screening and electrostatics require a self-consistent $\mathcal{T}(E,V)$ treatment [24, 25].

Within that controlled scope, the paper has three objectives. First, it quantifies the projection error across an entire smooth power-efficiency Pareto front rather than at a single selected optimum. Second, it reports stochastic variability in both spectral and Hamiltonian searches. Third, it tests chain length across the actual target set, enlarged bounds and simple bias-potential prescriptions. Finite-bias reservoir occupations are essential here because the Pareto targets are defined at nonzero power and at a specific operating load; fitting a spectrum only through equilibrium coefficients would not guarantee preservation of power and efficiency at that finite-load operating point.

The novelty is therefore not a new thermodynamic upper bound or a new optimum transmission family. Those benchmark questions are already well developed. Instead, the present work asks a different inverse-design question: after a Pareto-optimal spectrum has been identified in a flexible function space, how much of that front survives projection onto a short Hamiltonian with bounded microscopic parameters? By reporting the projection error along the front, rather than at one selected operating point, and by separating stochastic front uncertainty from Hamiltonian projection error and finite-bias model incompleteness, the calculation supplies a realizability layer between abstract transmission optimization and device-specific modeling.

Energy-dependent transmission also provides continuity with earlier mesoscopic thermoelectric work. Nonlinear Seebeck and Peltier response in quantum point contacts was formulated beyond linear response in [26], while one-dimensional resonant transmission was used to examine how resonance position and width control thermoelectric performance in [27]. The present work addresses the complementary inverse problem: rather than evaluating the thermoelectric response of a prescribed scattering structure, it asks whether spectra selected by finite-power Pareto optimization can be realized by a finite, constrained tight-binding Hamiltonian.

## 2. Methods

### 2.1. Exact reservoir currents with a frozen scattering Hamiltonian

The hot and cold reservoirs have $T_\mathrm{h} > T_\mathrm{c}$, $\mu_\mathrm{h} = 0$ and $\mu_\mathrm{c} = \Delta\mu > 0$. The particle current from hot to cold is

$$I_N = \frac{2}{h}\int \mathrm{d}E\,\mathcal{T}(E)\,[f_\mathrm{h}(E) - f_\mathrm{c}(E)] \tag{1}$$

where $f_\alpha(E) = [1+\exp((E-\mu_\alpha)/(k_\mathrm{B}T_\alpha))]^{-1}$. The hot-reservoir heat current is

$$J_\mathrm{h}^Q = \frac{2}{h}\int \mathrm{d}E\,(E-\mu_\mathrm{h})\,\mathcal{T}(E)\,[f_\mathrm{h}(E) - f_\mathrm{c}(E)]\,. \tag{2}$$

Delivered electrical power and efficiency are

$$P = \Delta\mu I_N, \qquad \eta = \frac{P}{J_\mathrm{h}^Q}, \qquad \eta_\mathrm{C} = 1 - \frac{T_\mathrm{c}}{T_\mathrm{h}}. \tag{3}$$

For every retained heat-engine operating point we require $P > 0$, $J_\mathrm{h}^Q > 0$, $0 \leqslant \eta \leqslant \eta_\mathrm{C}$, and non-negative entropy production.

Throughout the main Pareto optimization the reservoir Fermi functions are evaluated at finite voltage and temperature bias, while the central Hamiltonian and hence $\mathcal{T}(E)$ are frozen. The finite-bias occupations are not merely a numerical detail: they define the nonzero-power Pareto target and the load at which the projected spectrum is judged. We therefore use the term static-scattering finite-bias benchmark rather than device-level finite-bias transport. This approximation is controlled only when the bias-induced electrostatic rearrangement of the scatterer is negligible over the operating window, for example because screening is strong and most of the voltage drop occurs outside the active region. It is not a linear-response restriction on the reservoir integrals, but it is a serious restriction on the scattering problem. Self-consistent charging, voltage-drop profiles and interactions generate $\mathcal{T}(E,V)$ and can change the

predicted operating point [17, 23–25]. Section 3.6 is therefore part of the main validity analysis, not an auxiliary cosmetic test.

### 2.2. Spectral and Hamiltonian design spaces

The analytic reference families are

$$\mathcal{T}_L(E) = \frac{\Gamma^2}{(E-E_0)^2+\Gamma^2} \tag{4}$$

$$\mathcal{T}_{\mathrm{QPC}}(E) = \left[1+\mathrm{e}^{-(E-E_0)/\delta}\right]^{-1} \tag{5}$$

and a standard Fano form [28]. A smooth spectral target is described by eight natural-cubic-spline control amplitudes over $E/(k_{\mathrm{B}}T_{\mathrm{h}}) \in [-4, 11]$, with a logistic map enforcing $0 \leqslant \mathcal{T} \leqslant 1$.

For a non-interacting coherent $N$-site tight-binding chain,

$$H_N = \sum_{i=1}^{N} \epsilon_i |i\rangle\langle i| + \sum_{i=1}^{N-1} (t_i |i\rangle\langle i+1| + \mathrm{h.c.}). \tag{6}$$

The wide-band lead self-energies are

$$\Sigma_L^r = -\frac{\mathrm{i}\Gamma_L}{2}|1\rangle\langle 1|, \qquad \Sigma_R^r = -\frac{\mathrm{i}\Gamma_R}{2}|N\rangle\langle N| \tag{7}$$

so that

$$\begin{aligned} G^r(E) &= [EI - H_N - \Sigma_L^r - \Sigma_R^r]^{-1} \\ \mathcal{T}_N(E) &= \Gamma_L\Gamma_R |G_{1N}^r(E)|^2 \end{aligned} . \tag{8}$$

The $N = 5$ projection has 11 Hamiltonian parameters and one jointly optimized load. These are phenomenological search bounds, not universal quantum-dot constraints: $\epsilon_i/(k_{\mathrm{B}}T_{\mathrm{h}}) \in [-1, 8]$, $t_i/(k_{\mathrm{B}}T_{\mathrm{h}}) \in [0.05, 3]$ and $\Gamma_{L,R}/(k_{\mathrm{B}}T_{\mathrm{h}}) \in [0.05, 3]$. For Target 30 the onsite interval is widened to $[-2, 16]$ and the hopping interval to $[0.05, 6]$; contacts and load bounds remain unchanged. The original best solution is explicitly retained as a feasible incumbent in the enlarged search.

### 2.3. Optimization and reproducibility

All calculations use $k_{\mathrm{B}}T_{\mathrm{h}} = 1$, $T_{\mathrm{c}}/T_{\mathrm{h}} = 0.6$, $\mu_{\mathrm{h}} = 0$, and $\Delta\mu/(k_{\mathrm{B}}T_{\mathrm{h}}) \in [0.01, 3]$. The power normalization is

$$P_0 = 2(k_{\mathrm{B}}T_{\mathrm{h}})^2/h. \tag{9}$$

Eight natural-cubic-spline amplitudes on equally spaced knots in $[-4, 11]$ lie in $[-12, 12]$. Their logistic map defines the transmission, with constant continuation of the spline argument beyond the endpoints. This specified function space restricts the optimized front; global Pareto optimality is not proved.

NSGA-II [13] uses population 72, 48 generations, simulated-binary crossover probability 0.9 and distribution index 15, and polynomial mutation probability 1/9 with distribution index 20. The five seeds are 311, 517, 823, 1103 and 1601. Hypervolume uses normalized coordinates $x = (P/P_0)/0.0507$, $y = \eta/\eta_{\mathrm{C}}$ and reference $(0, 0)$, and is computed before target refinement. Thirty points are initialized at equally spaced polygonal arc lengths between 3% and 97% of the pooled nondominated front. Spline amplitudes and load are interpolated, and each resulting actual power is held fixed while SLSQP maximizes efficiency from two starts. SLSQP uses at most 250 iterations and tolerance $10^{-10}$; an improved point is retained only if its power residual is below $10^{-6}$. The refined target spectrum and load, rather than interpolated performance coordinates, define each inverse-design target.

Every reported target, chain, curve and table belongs to this single regenerated numerical experiment. Target indices identify this dataset; the archived spectra, fitted parameters, seeds and code accompany the results.

### 2.4. Joint spectral and operating-point projection

The transport-weighted spectral loss is

$$L_{\mathrm{spec}}^{(j)} = \frac{\int \mathrm{d}E\, w_j(E)\left[\mathcal{T}_N(E) - \mathcal{T}_j(E)\right]^2}{\int \mathrm{d}E\, w_j(E)}; \quad w_j = |f_{\mathrm{h}} - f_{\mathrm{c}}| + 0.01\exp\left[-(E/8)^2/2\right] \tag{10}$$

Here energies in the weight are dimensionless, the Fermi functions use the target load and the spectral-loss integrals are defined on the fixed interval $[-16, 24]$. The operating-point distance and common objective are

$$d_j^2 = \left[\frac{(P/P_0) - (P/P_0)_j}{0.0507}\right]^2 + \left[\frac{\eta - \eta_j}{\eta_{\mathrm{C}}}\right]^2, F_N = L_{\mathrm{spec}} + 0.03 d_j^2. \tag{11}$$

Each of the 30 targets is independently fitted for every $N = 3, \ldots, 8$, giving 180 projections. Two differential-evolution runs per projection use population multiplier 6, 60 generations, tolerance $10^{-7}$ and no built-in polishing, followed by bounded least-squares refinement of the residual vector defining the same objective. Local refinement uses at most 250 function evaluations, function and step tolerances $10^{-10}$ and gradient tolerance $10^{-9}$. Seeds are $20\,260\,930 + 1000\,(j-1) + 100N + k$, $k = 0, 1$. Both run objectives are archived; the lower-objective solution is retained. Local solvers that reach their budget are retained as best-found solutions and are not labeled converged global optima. The widened Target-30 search uses the same seeds and budgets, includes the original incumbent in both searches and retains it if no improvement is found.

The optimization quadrature uses 2001 energies over $[-16, 24]$. Candidate fits are checked on 8001 points and refined there if power, normalized efficiency or spectral-loss differences exceed $2 \times 10^{-5}$, $2 \times 10^{-4}$ or $2 \times 10^{-5}$, respectively. All fits are then evaluated on 16 001 points. Final projection-table values use an independent adaptive Gauss–Kronrod vector integration, split around the complex poles of the open-chain Hamiltonian as well as the spline knots. Relative tolerances $10^{-9}$ and $10^{-10}$ are compared. A detected narrow-resonance discrepancy triggers composite-mesh local refinement followed by repeated adaptive verification. The supplied diagnostics preserve the uniform-grid discrepancies; a uniform energy grid alone is not treated as adequate validation.

For complexity reporting, a chain is called successful when both $L_{\mathrm{spec}} \leqslant 10^{-3}$ and $d^2 \leqslant 10^{-3}$. This declared operational tolerance is a reporting choice, not a universal physical threshold. We report the smallest successful tested $N$, without asserting that shorter chains are impossible. No success through eight sites is labeled unresolved under the present bounds and budget.

## 3. Results

### 3.1. Independent transport and numerical checks

The tridiagonal end-to-end Green-function recurrence agrees with direct matrix inversion to a maximum absolute transmission error of $7.3 \times 10^{-17}$ in the archived random-Hamiltonian check. A sharp high-pass filter has lower edge $E^* = \Delta\mu/\eta_{\mathrm{C}}$. Analytic integration of its particle current and scalar optimization of the load give $P_{\max}/P_0 = 0.05061547$ at $\Delta\mu/(k_{\mathrm{B}}T_{\mathrm{h}}) = 0.457823$, consistent with the commonly quoted rounded scale 0.0507 [8, 9]. The scale 0.0507 is retained only as the declared distance normalization.

Independent small-perturbation checks recover the equilibrium $L_0$ and $L_1$ current derivatives with relative errors $1.8 \times 10^{-12}$ and $1.1 \times 10^{-11}$. Every retained chain operating point satisfies positive delivered power and hot heat current, $0 < \eta/\eta_{\mathrm{C}} \leqslant 1$, nonnegative transmission not exceeding unity, and nonnegative entropy production. The smallest dimensionless entropy production is 0.003 721.

Two adaptive integration tolerances differ by at most $2.9 \times 10^{-16}$ in $P/P_0$ and $1.6 \times 10^{-14}$ in $\eta/\eta_{\mathrm{C}}$. The uniform-grid check found one significant narrow-resonance discrepancy, which was explicitly refined and verified. These checks validate integral evaluation at retained solutions; they do not certify global optimization.

### 3.2. Stochastic uncertainty and target construction

The five normalized hypervolumes are 0.619 338, 0.609 628, 0.557 600, 0.532 976, 0.592 846; their mean and sample standard deviation are 0.582 478 and 0.036 306. This visible spread establishes that the finite NSGA-II budget remains optimizer-sensitive. Figure 1 shows each unrefined seed front and the pooled, equal-power-refined targets. No independent IGD reference is constructed from the same runs.

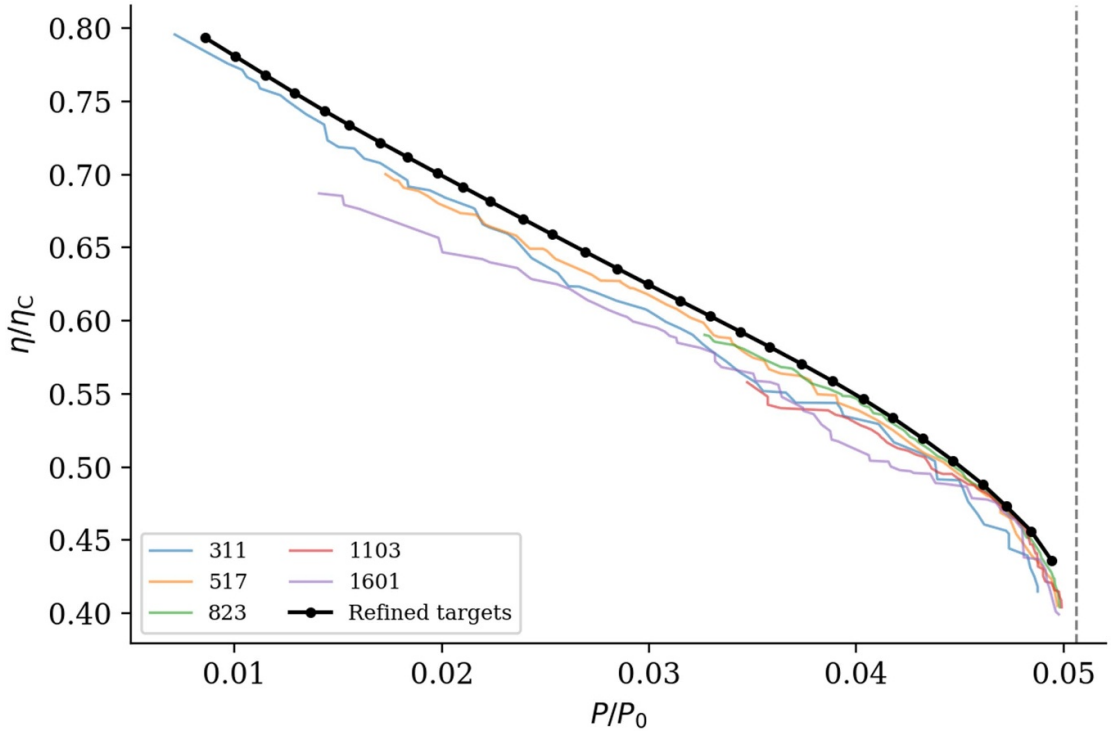


**Figure 1.** Independent smooth-spectrum seed fronts and the refined target set. The dashed line is the independently optimized sharp-filter maximum power.

### 3.3. Five-site projection across the front

Figures 2 and 3 separate operating-point displacement from spectral approximation. The median five-site $L_{\mathrm{spec}}$ is 0.000 25; the median absolute errors are 0.000 389 in $P/P_0$ and 0.0208 in $\eta/\eta_{\mathrm{C}}$. Spectral fits can therefore look close while retaining a material efficiency displacement. The soft objective penalty $0.03d^2$ is not a hard constraint preserving power or efficiency. Table 1 reports representative values without describing their operating points as indistinguishable.

### 3.4. Chain length on the actual target front

Every chain length is fitted to every actual target, replacing the artificial-window-only complexity test. Figure 4 and table 2 show the spectral losses and the smallest successful tested chain lengths under the joint tolerance. The complete 180-row table includes both errors, fitted loads and all Hamiltonian parameters in the accompanying files. Adjacent lengths are not guaranteed to give monotonic best-found errors: each search is nonconvex and the serial-chain parameterizations are not treated as nested feasible sets.

The lowest-power targets meet the chosen tolerance with shorter tested chains, whereas the upper-power end demands more degrees of freedom or remains unresolved. This is a computational realizability map under stated search conditions. It is not a lower bound on the mathematically required chain length or evidence of a universal convergence exponent.

### 3.5. Enlarged-box test at Target 30

The expanded onsite and hopping ranges contain the original feasible set, so the original solution must remain an available candidate. With that incumbent retained, the best-found combined objective decreases by 0.247%. However, the spectral term decreases while $d^2$ increases (table 3). The test therefore supports a small trade-off improvement in the stated objective; it does not demonstrate simultaneous improvement in both physical diagnostics or a bound-independent architectural limit. Contact broadenings remain constrained, and a larger search budget could change the best-found result.

### 3.6. Numerical bias-profile sensitivity

The saved five-site Hamiltonian for Target 18 is used without refitting. The three prescriptions are frozen onsite energies, a rigid half-bias shift $\epsilon_i \to \epsilon_i + \Delta\mu/2$, and a linear ramp $\epsilon_i \to \epsilon_i + (i-1)\Delta\mu/(N-1)$. Lead broadenings are held fixed. A 1201-point scan over dimensionless loads $[0.001, 3]$ identifies the efficiency maximum in the heat-engine regime, followed by bounded scalar refinement of its local bracket.

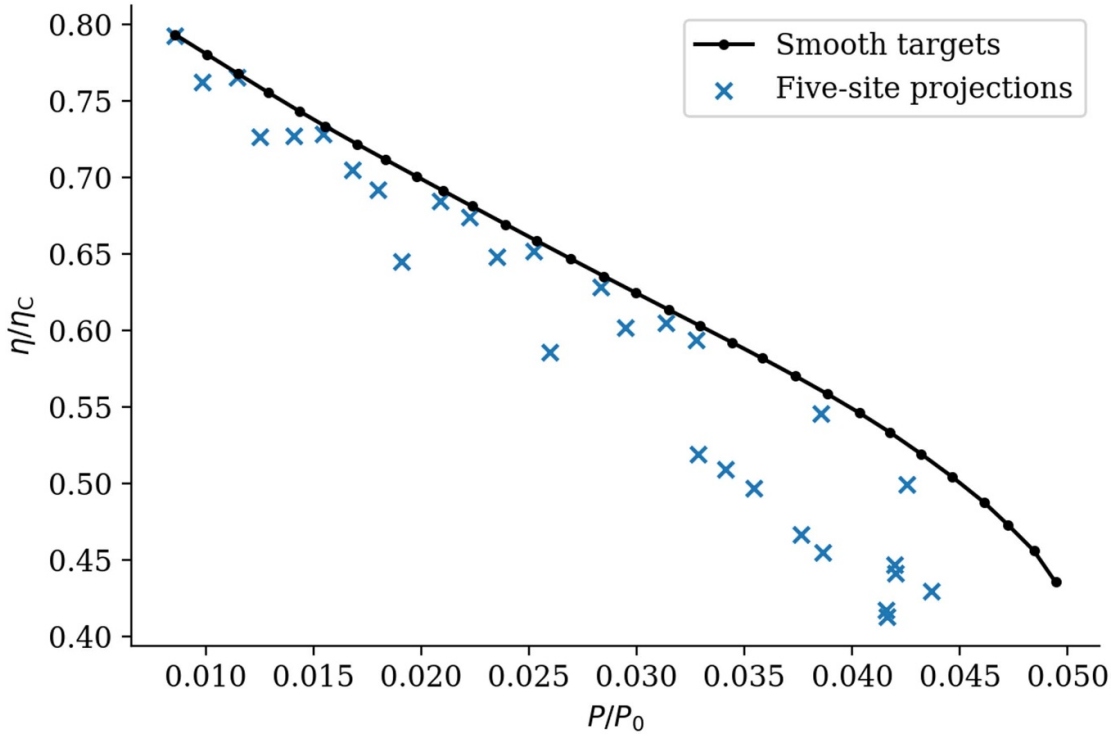


**Figure 2.** The same 30 smooth-spectrum targets and their five-site projections at each fitted load.

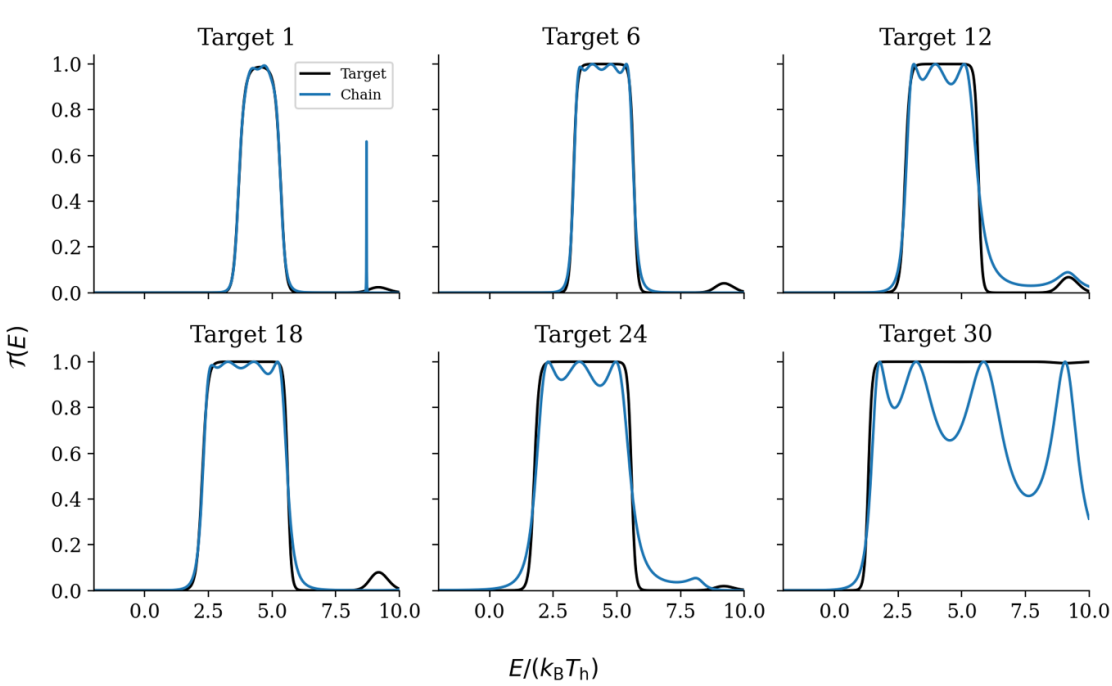


**Figure 3.** Representative target and five-site transmission spectra; all spectra use the archived Hamiltonians.

Peak efficiency and the power at that same load are reported separately from maximum power. Figure 5 compares the power–efficiency curves for the three bias prescriptions, and table 4 lists their peak efficiencies, the corresponding powers and the shifts relative to frozen scattering.

The shifts quantify the sensitivity to assumed electrostatics. None of these prescribed profiles solves charging or screening self-consistently. The main projections remain finite-bias Landauer benchmarks with frozen scattering, rather than validated biased devices.

**Table 1.** Representative five-site projections evaluated by adaptive integration.

| Target | $P_t/P_0$ | $\eta_t/\eta_C$ | $P_N/P_0$ | $\eta_N/\eta_C$ | $L_{spec}$ |
|---|---|---|---|---|---|
| 1 | 0.008 576 | 0.793 51 | 0.008 565 | 0.792 91 | $1.15 \times 10^{-05}$ |
| 6 | 0.015 527 | 0.733 79 | 0.015 425 | 0.728 29 | $2.58 \times 10^{-05}$ |
| 12 | 0.023 916 | 0.669 57 | 0.023 516 | 0.648 26 | 0.000 374 |
| 18 | 0.032 946 | 0.603 15 | 0.032 765 | 0.593 83 | 0.000 126 |
| 24 | 0.041 766 | 0.533 54 | 0.038 653 | 0.455 15 | 0.001 14 |
| 30 | 0.049 443 | 0.435 74 | 0.041 614 | 0.413 06 | 0.0279 |

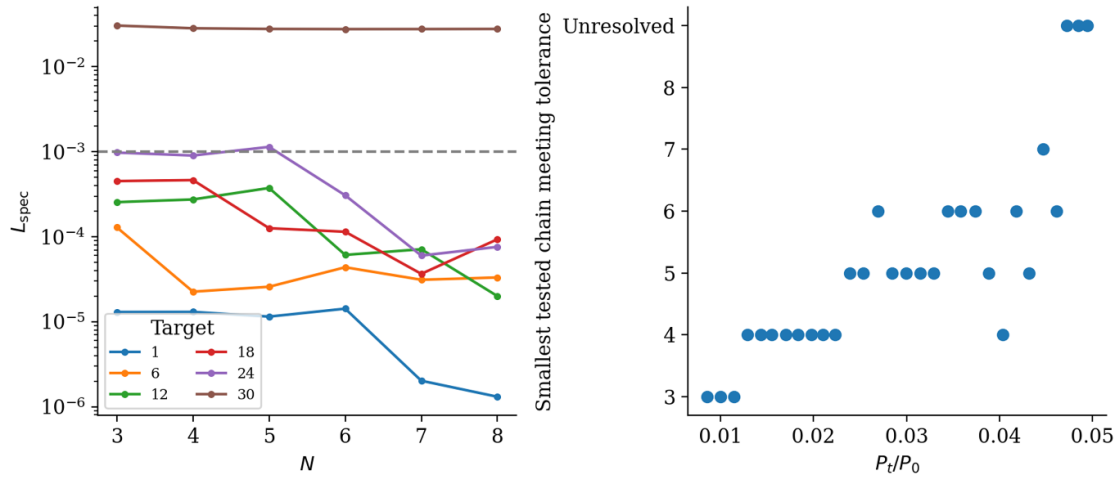


**Figure 4.** Chain-length scans for representative actual targets (left) and the smallest successful tested length under both declared tolerances (right). Unresolved means that no retained solution met both tolerances.

**Table 2.** Spectral losses on actual Pareto targets and the smallest successful tested length.

| Target | $N = 3$ | $N = 4$ | $N = 5$ | $N = 6$ | $N = 7$ | $N = 8$ | Successful $N$ |
|---|---|---|---|---|---|---|---|
| 1 | $1.3 \times 10^{-05}$ | $1.3 \times 10^{-05}$ | $1.15 \times 10^{-05}$ | $1.42 \times 10^{-05}$ | $2.02 \times 10^{-06}$ | $1.31 \times 10^{-06}$ | 3 |
| 6 | 0.000 129 | $2.25 \times 10^{-05}$ | $2.58 \times 10^{-05}$ | $4.37 \times 10^{-05}$ | $3.11 \times 10^{-05}$ | $3.31 \times 10^{-05}$ | 4 |
| 12 | 0.000 255 | 0.000 274 | 0.000 374 | $6.1 \times 10^{-05}$ | $7.12 \times 10^{-05}$ | $2 \times 10^{-05}$ | 5 |
| 18 | 0.000 451 | 0.000 463 | 0.000 126 | 0.000 114 | $3.65 \times 10^{-05}$ | $9.32 \times 10^{-05}$ | 5 |
| 24 | 0.000 978 | 0.000 902 | 0.001 14 | 0.000 307 | $5.99 \times 10^{-05}$ | $7.59 \times 10^{-05}$ | 6 |
| 30 | 0.0305 | 0.0284 | 0.0279 | 0.0277 | 0.0278 | 0.0279 | Unresolved |

**Table 3.** Target-30 five-site bound sensitivity with retained incumbent; values from adaptive integration.

| Bounds | $L_{spec}$ | $d^2$ | $F_5$ | $P/P_0$ | $\eta/\eta_C$ |
|---|---|---|---|---|---|
| Original | 0.0279 | 0.0244 | 0.0286 | 0.041 614 | 0.413 06 |
| Widened | 0.0277 | 0.0262 | 0.0285 | 0.041 335 | 0.411 33 |

### 3.7. One-sided shrinking-window Carnot test

At dimensionless load $\Delta\mu = 0.6$, the equal-occupation crossing is $E^* = \Delta\mu/\eta_C = 1.5$. We integrate the rectangular transmission on $[E^*, E^* + \delta]$. The window is one-sided: symmetric placement around the crossing allows opposing particle currents and does not implement the stated heat-engine limit. Figure 6 and table 5 show that efficiency approaches Carnot while power vanishes.

Near the crossing, $f_h - f_c$ is proportional to $E - E^*$, so particle current and power scale as $\delta^2$, while $1 - \eta/\eta_C$ is of order $\delta$. The limit demonstrates reversibility at vanishing power and agrees with finite-power constraints [8, 9]. It does not assert that a bounded finite chain realizes an arbitrarily narrow ideal rectangular filter.

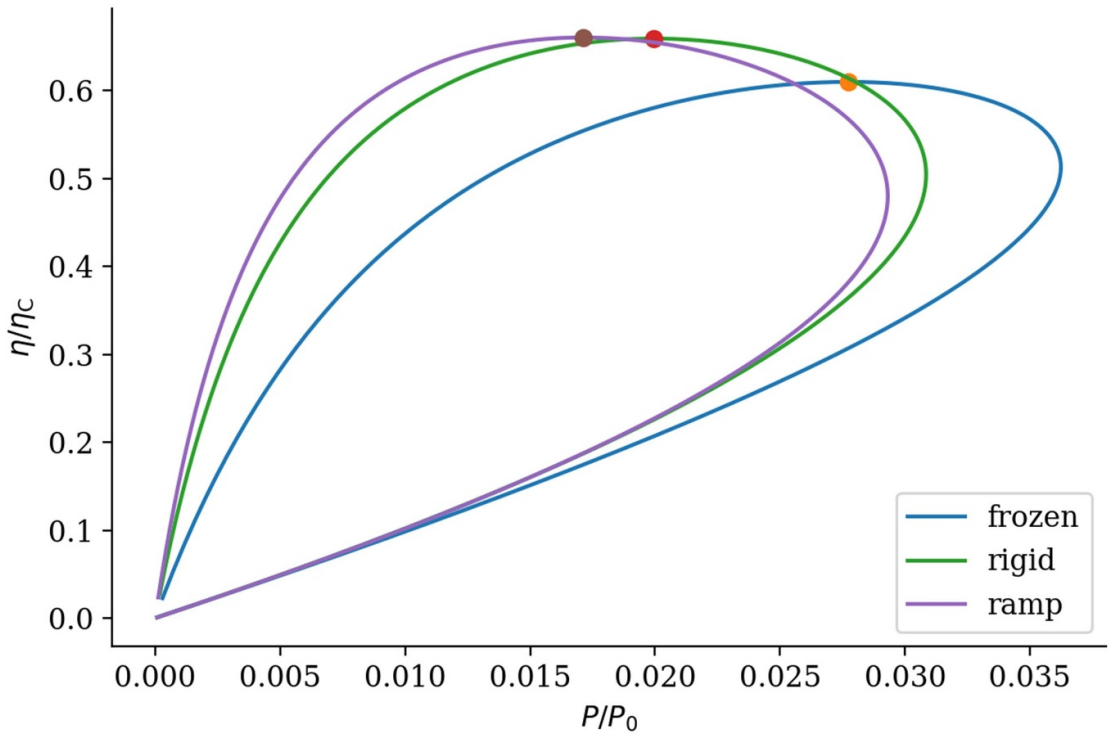


**Figure 5.** Bias prescriptions for the same archived Target-18 five-site Hamiltonian. Dots locate peak efficiency within the stated scan interval.

**Table 4.** Peak efficiency and corresponding power, with shifts relative to frozen scattering.

| Prescription | Peak $\eta/\eta_C$ | $P/P_0$ at peak | $\Delta(\eta/\eta_C)$ | $\Delta(P/P_0)$ |
|---|---|---|---|---|
| Frozen | 0.610 012 | 0.027 743 | +0.000 000 | +0.000 000 |
| Rigid | 0.659 247 | 0.019 962 | +0.049 235 | −0.007 781 |
| Ramp | 0.660 511 | 0.017 130 | +0.050 498 | −0.010 613 |

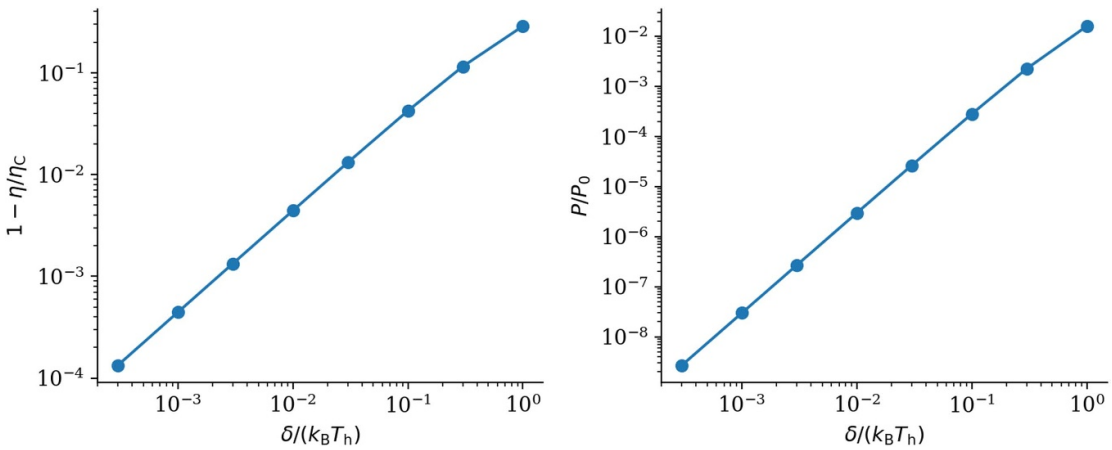


**Figure 6.** Direct adaptive integration of a shrinking one-sided transmission window: efficiency deficit (left) and delivered power (right).

### 3.8. Current-fluctuation diagnostic

For the same noninteracting, spin-degenerate transport model, the symmetrized zero-frequency charge-current noise is

$$S_I = \frac{4e^2}{h}\int \mathrm{d}E\left\{\mathcal{T}\left[f_\mathrm{h}\left(1-f_\mathrm{h}\right)+f_\mathrm{c}\left(1-f_\mathrm{c}\right)\right]+\mathcal{T}\left(1-\mathcal{T}\right)\left(f_\mathrm{h}-f_\mathrm{c}\right)^2\right\}. \tag{12}$$

**Table 5.** Shrinking-window test at fixed load 0.6; widths are in units of $k_B T_h$.

| Width | $P/P_0$ | $\eta/\eta_C$ |
|---|---|---|
| 1.0 | 0.0158661 | 0.71289704 |
| 0.3 | 0.0022467 | 0.88482022 |
| 0.1 | 0.000281 618 | 0.95774648 |
| 0.03 | $2.63929 \times 10^{-05}$ | 0.98686995 |
| 0.01 | $2.9661 \times 10^{-06}$ | 0.99557834 |
| 0.003 | $2.680\,09 \times 10^{-07}$ | 0.99866872 |
| 0.001 | $2.98125 \times 10^{-08}$ | 0.99955578 |
| 0.0003 | $2.68418 \times 10^{-09}$ | 0.99986669 |

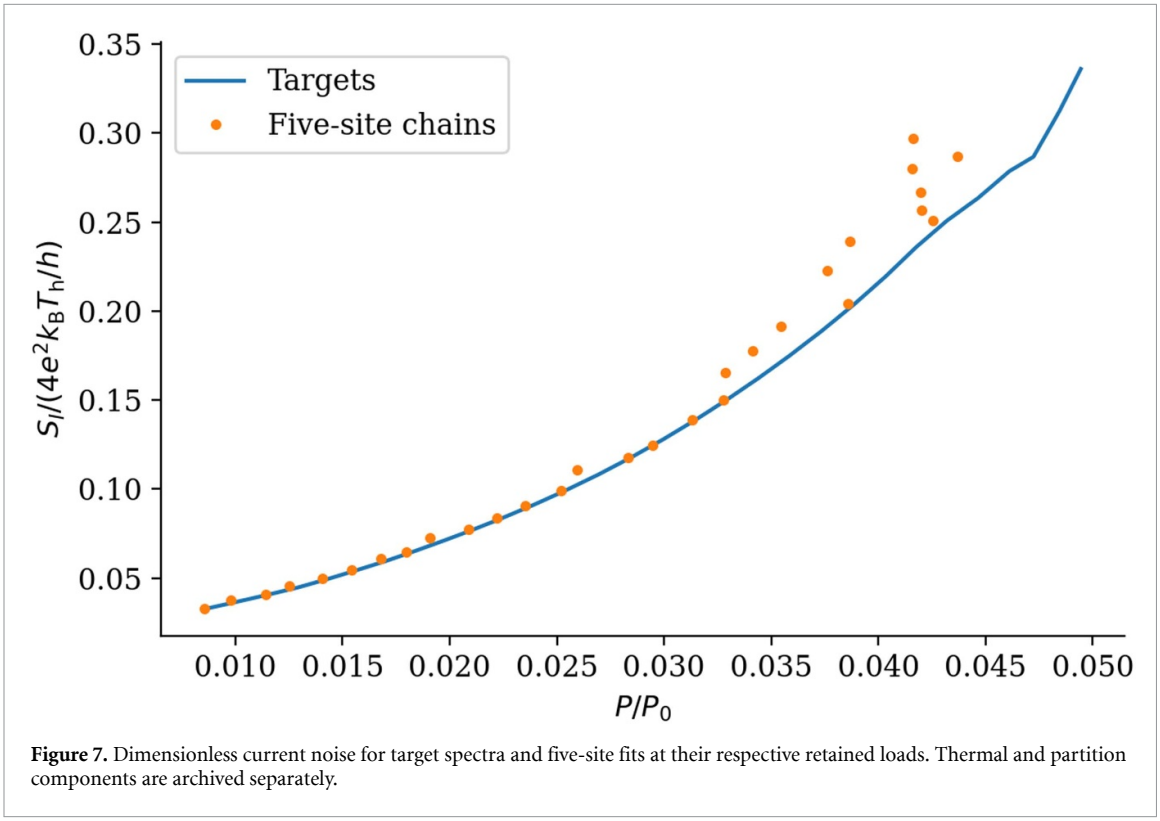


**Figure 7.** Dimensionless current noise for target spectra and five-site fits at their respective retained loads. Thermal and partition components are archived separately.

The first contribution is thermal noise and the second is partition noise. Figure 7 and the accompanying component table evaluate both at each target's or fitted chain's own archived load. This comparison does not hold the mean operating point exactly fixed and is a diagnostic, not a fluctuation-minimization result. A three-objective inverse design would be needed to control noise as well as mean power and efficiency. Boxcar transmissions have a distinguished role in fixed-mean fluctuation optimization [29], and coherent uncertainty relations must be used with their stated hypotheses [30].

## 4. Discussion

The numerical contribution is the projection map from flexible spectra to bounded microscopic Hamiltonians, rather than a new optimum transmission family. The rebuilt dataset makes three uncertainties inspectable: independent spectral and Hamiltonian searches quantify optimizer variability; joint spectral and operating-point residuals quantify projection quality; and prescribed bias profiles expose model sensitivity to omitted electrostatics. Optimizer variability is reported, but cannot be completely separated from an architectural floor without substantially stronger global optimization.

Finite resonant chains can approximate favorable energy filters, yet a small weighted spectral error does not by itself preserve efficiency at a selected load. Broad high-power spectra are particularly demanding under the stated contacts and Hamiltonian bounds. The all-target chain-length scan is more direct than an artificial-window benchmark, but its smallest successful tested lengths are achievable

examples, not proofs of minimal Hamiltonian complexity. The widened-box result further shows why individual diagnostics and the optimized composite objective must be distinguished.

Experimental nonlinear thermoelectric and quantum-dot heat engines [19–22], interacting transport theories [17, 18, 23, 31] and fluctuation-based performance measures [29, 30, 32] motivate further device modeling. They do not validate these static single-particle Hamiltonians. Self-consistent electrostatics, charging, many-body correlations and microscopic parasitic heat transport remain outside the forward problem. Differentiable NEGF approaches [12] may help optimize such richer models, provided their physical approximations are independently assessed.

## 5. Conclusions

Thirty targets from one explicitly specified smooth-spectrum experiment have been projected onto every coherent chain length from three to eight sites. Independent seeds, archived Hamiltonians and pole-aware adaptive integration make the numerical residuals auditable. Five-site spectral agreement is often good, but the recomputed operating-point errors rule out claiming uniformly near-perfect thermodynamic reproduction. A joint tolerance identifies successful tested chain lengths across the front; the highest-power targets remain unresolved within the tested search conditions.

Retaining the feasible incumbent in the widened Target-30 search produces a small reduction in the composite objective, accompanied by an increase in operating-point distance. The numerical one-sided-window test approaches Carnot only as power vanishes, while the bias-profile table quantifies substantial shifts for the same Hamiltonian. These results strengthen the computational baseline while retaining its precise scope: exact finite-bias reservoir occupations with frozen scattering, without self-consistent device electrostatics. Neither a universal architecture limit nor a new thermodynamic bound is claimed.

## Data availability statement

All data that support the findings of this study are included within the article (and any supplementary files).

Supplementary code and data available at https://doi.org/10.1088/1402-4896/aeb906/data1 [33].

## Funding

This research received no financial support.

## Author contribution

Mustafa Ali Çipiloğlu 0009-0004-6692-238X
Conceptualization, Data curation, Formal analysis, Investigation, Methodology, Validation, Writing – original draft, Writing – review & editing

## References

[1] Landauer R 1957 *IBM J. Res. Dev.* **1** 223–31
[2] Büttiker M 1986 *Phys. Rev. Lett.* **57** 1761–4
[3] Sivan U and Imry Y 1986 *Phys. Rev. B* **33** 551–8
[4] Giazotto F, Heikkilä T T, Luukanen A, Savin A M and Pekola J P 2006 *Rev. Mod. Phys.* **78** 217–74
[5] Dubi Y and Di Ventra M 2011 *Rev. Mod. Phys.* **83** 131–55
[6] Benenti G, Casati G, Saito K and Whitney R S 2017 *Phys. Rep.* **694** 1–124
[7] Mahan G D and Sofo J O 1996 *Proc. Natl Acad. Sci. USA* **93** 7436–9
[8] Whitney R S 2014 *Phys. Rev. Lett.* **112** 130601
[9] Whitney R S 2015 *Phys. Rev. B* **91** 115425
[10] Ding S, Chen X, Xu Y and Duan W 2023 *npj Comput. Mater.* **9** 189
[11] Chrirou C, El Allati A and Whitney R S 2026 *Phys. Rev. B* **113** 155304
[12] Zhouyin Z, Chen X, Zhang P, Wang J and Wang L 2023 *Phys. Rev. B* **108** 195143
[13] Deb K, Pratap A, Agarwal S and Meyarivan T 2002 *IEEE Trans. Evol. Comput.* **6** 182–97
[14] Beenakker C W J 1991 *Phys. Rev. B* **44** 1646–56
[15] van der Wiel W G, De Franceschi S, Elzerman J M, Fujisawa T, Tarucha S and Kouwenhoven L P 2003 *Rev. Mod. Phys.* **75** 1–22

[16] Goldhaber-Gordon D, Shtrikman H, Mahalu D, Abusch-Magder D, Meirav U and Kastner M A 1998 *Nature* **391** 156–9
[17] Meir Y and Wingreen N S 1992 *Phys. Rev. Lett.* **68** 2512–5
[18] Sothmann B, Sánchez R and Jordan A N 2015 *Nanotechnology* **26** 032001
[19] Fahlvik Svensson S, Hoffmann E A, Nakpathomkun N, Wu P M, Xu H Q, Nilsson H A, Sánchez D, Kashcheyevs V and Linke H 2013 *New J. Phys.* **15** 105011
[20] Svilans A, Burke A M, Fahlvik Svensson S, Leijnse M and Linke H 2016 *Physica E* **82** 34–38
[21] Josefsson M, Svilans A, Burke A M, Hoffmann E A, Fahlvik S, Thelander C, Leijnse M and Linke H 2018 *Nat. Nanotechnol.* **13** 920–4
[22] Majidi D, Josefsson M, Kumar M, Leijnse M, Samuelson L, Courtois H, Winkelmann C B and Maisi V F 2022 *Nano Lett.* **22** 630–5
[23] Sierra M A and Sánchez D 2014 *Phys. Rev. B* **90** 115313
[24] Sánchez D and López R 2013 *Phys. Rev. Lett.* **110** 026804
[25] Sánchez D and López R 2016 *C. R. Physique* **17** 1060–71
[26] Çipiloğlu M A, Turgut S and Tomak M 2004 Nonlinear Seebeck and Peltier effects in quantum point contacts *Phys. Status Solidi b* **241** 2575–85
[27] Çipiloğlu M A and Turgut S 2009 Figure of merit of one-dimensional resonant transmission systems in the quantum regime *Math. Comput. Appl.* **14** 13–19
[28] Fano U 1961 *Phys. Rev.* **124** 1866–78
[29] Timpanaro A M, Guarnieri G and Landi G T 2025 *Phys. Rev. B* **111** 014301
[30] Brandner K and Saito K 2025 *Phys. Rev. Lett.* **135** 046302
[31] Thierschmann H, Sánchez R, Sothmann B, Arnold F, Heyn C, Hansen W, Buhmann H and Molenkamp L W 2015 *Nat. Nanotechnol.* **10** 854–8
[32] Kheradsoud S, Dashti N, Misiorny M, Potts P P, Splettstoesser J and Samuelsson P 2019 *Entropy* **21** 777
[33] Çipiloğlu M A 2026 *Supplementary code and data* (https://doi.org/10.1088/1402-4896/aeb906/data1)